

Engineering Quantum Emission with Mie Voids

Yuchao Fu¹, Ilia Lykov¹, Sergejs Boroviks¹, Nai-Quan Zhu², Tianyue Li³, Siarhei Zavatski¹, Makhlad Chahid⁴, Olivier J. F. Martin¹**

¹ *Nanophotonics and Metrology Laboratory, Swiss Federal Institute of Technology Lausanne (EPFL); 1015 Lausanne, Switzerland.*

² *School of Electronic Information and Electrical Engineering, Shanghai Jiao Tong University (SJTU); 200240 Shanghai, China.*

³ *Department of Physics, The Hong Kong University of Science and Technology; 999077, Hong Kong.*

⁴ *Center of MicroNanoTechnology, Swiss Federal Institute of Technology Lausanne (EPFL); 1015 Lausanne, Switzerland.*

**Corresponding author. Email: yuchao.fu@epfl.ch ; olivier.martin@epfl.ch*

Abstract

Spontaneous emission, as a fundamental radiative process and a versatile information carrier, plays a vital role in light-emitting devices, optical information modulation and encryption, super-resolution fluorescence imaging and nano sensing. Engineering the photonic environment surrounding quantum emitters can enhance their emission characteristics. However, simultaneously achieving precise control over both excitation enhancement and quantum-yield modulation at the nanoscale remains elusive, highlighting substantial room for advancing the precised engineering of quantum emission. Here, we introduce silicon Mie voids — air-defined cavities that invert the conventional solid-particle geometry — to achieve independent tuning of quantum emission within an individual subwavelength structure, while minimizing optical losses. Full-wave simulations and experiments on both gradient and uniform Mie-void arrays jointly validate this quantitative framework for emission tuning, which disentangles excitation enhancement arising from local field confinement in air and quantum-yield enhancement resulting from strengthened emitter–resonator coupling, while confirming the accelerated radiative decay enabled by the void configuration. Leveraging this flexible mechanism, we realize a bimodal nanophotonic pattern with near-diffraction-limited pixels that encode the EPFL logo in the bright field and the SJTU logo in both dark field and photoluminescence micrographs. These results establish Mie voids as a powerful platform for programmable, high-density multimodal displays and open new avenues for advancing state-of-the-art nanophotonic devices.

Introduction

Tailoring light–matter interactions at the nanoscale has become central to modern photonics, enabling unprecedented advances in spontaneous emission control, nonlinear optics, and quantum information processing¹⁻⁴. High-index dielectric nanostructures supporting Mie resonances offer a highly versatile alternative to plasmonic systems, enabling strong confinement of optical modes with reduced absorption losses, generating high-purity structural colors and exhibiting novel optical states such as anapoles, Fano resonances, and bound states in the continuum (BICs)⁵⁻¹³. These effects originate from the interplay between electric and magnetic multipoles induced by optically driven displacement currents inside high-index dielectric particles^{6,8}. Mie resonators also enable interference-driven scattering anisotropy, exemplified by forward–backward asymmetry under Kerker conditions¹⁴⁻¹⁷. The optical response of all-dielectric nanostructures can be well described by the Mie theory¹⁸. A particularly compelling recent advancement has been the emergence of all-dielectric Mie voids — nanoscale air-filled cavities embedded in high-index dielectrics — which invert the traditional solid-particle geometry while preserving multipolar Mie resonances¹⁹. By displacing the resonant field maxima from an optical lossy material region into the low-index air, all-dielectric Mie voids reduce absorptive losses to a negligible level, while simultaneously achieving tighter field confinement in air and extending the resonance spectral range toward the blue and even ultraviolet regimes^{19,20}. Compared to traditional metasurfaces composed of solid Mie scatterers^{5,6,21}, Mie voids provide an air-defined nanophotonic platform that introduces new degrees of freedom for engineering light–matter interactions at the nanoscale. Although this field of research is in its infancy, the potential of Mie voids for practical applications seems tremendous and has already recently been demonstrated for the detection of nanoplastics²². Here, we report for the first time a fully unexpected effect and demonstrate that vacuum – in the form of Mie voids – can also strongly modify the local optical density of state and control molecular quantum emission.

Spontaneous emission represents an intrinsic property of isolated emitters^{23,24}, and it can be profoundly modified by tailoring their surrounding photonic environment^{21,25}. By the virtue of the Purcell effect, the spontaneous emission rate of a quantum emitter is proportional to the local density of optical states (LDOS), and thus can be enhanced by embedding the emitter in a resonant structure with high quality factor (Q) and small mode volume (V_m)²⁶⁻³¹. Plasmonic nanostructures initially led this field by providing deeply subwavelength field confinement and

large optical LDOS, thereby yielding large Purcell factors; however, their observable quantum efficiencies are compromised by the quenching from intrinsic ohmic losses^{21,32-35}. Photonic crystal slabs enable record-high fluorescence enhancement (nearly 3000 -fold) through combined resonant excitation and directional extraction³⁶, and single-emitter studies coupling a tin-vacancy center in diamond to a photonic-crystal nanobeam cavity have achieved \sim 12-fold emission enhancement with a Purcell factor of 37³⁷, while hybrid photonic–plasmonic cavities combine strong plasmonic localization with high-Q photonic modes to realize narrowband and tunable emission enhancement³⁸. Yet, both approaches demand sophisticated nanofabrication and offer limited flexibility for spatially resolved emission control³⁶⁻³⁸. In contrast to their plasmonic counterparts, all-dielectric Mie resonators are comparatively facile to fabricate thanks to their larger feature sizes and can simultaneously support directional emission, flexible spatial arrangement, and lifetime shortening with reduced contributions from non-radiative decay^{15,39,40}. Recent progress in all-dielectric nanophotonic platforms, such as Fano metasurfaces and quasi-BIC metasurfaces, has also enabled nonlocal ultrahigh-Q resonances on large-area periodic structures that deliver strong Purcell enhancement together with angular control over far-field emission^{35,36,41-43}. Altogether, these studies pave the way for chip-scale, room-temperature emitters with engineered radiative lifetimes, directional luminescence, and on-demand spectral shaping, extending spontaneous emission control to practical applications in nanolasers and super-resolution imaging⁴⁴⁻⁴⁸.

Despite recent advances in Mie resonators and all-dielectric metasurface designs, these platforms still face some fundamental challenges, including the difficulty of simultaneously achieving precise and flexible control over both excitation enhancement and quantum yield enhancement, as well as spatially resolved emission control at the single-resonator scale. A particularly important limitation of most solid-particle Mie resonators is that their effective mode volume is largely confined within the high-index dielectric material^{2,6,49}, leading to intrinsically weak resonant coupling with quantum emitters residing in the surrounding low-index environment. Here, we propose the use of Mie voids to overcome this constraint through their complementary geometry, which localizes resonant electromagnetic fields predominantly in air and thereby facilitates stronger coupling of an external emitter to both cavity modes and radiation channels, while their unique mode profile further reduces the effective mode volume and enhances the optical LDOS^{19,50}. Besides, the geometric flexibility of Mie voids in shaping air-defined cavities enables quantum emission control with subwavelength spatial resolution, unlocking the potential for precisely orchestrating quantum emission responses. Yet, to the best

of our knowledge, there is no systematic study of how Mie voids tune quantum emission compared to solid dielectric resonators, and a quantitative framework linking void geometry, local-field-driven excitation enhancement, and resonance-mediated quantum yield enhancement is still lacking.

In this work, we focus on establishing a flexible and precise platform for tailoring quantum emission within the smallest possible submicron void volume. We systematically compare the scattering efficiency and multipole decompositions of conventional solid Mie particles versus air-defined Mie voids^{19,51,52}, revealing that the latter maintain similar modal content while offering enhanced near-field access. We also analyze the quantum emission tuning effect of Mie voids on dipolar emitters from two complementary perspectives⁵³: (i) excitation enhancement, driven by local field concentration within the void, and (ii) quantum yield enhancement, quantified via the Purcell factor, dielectric absorption, and far-field radiation efficiency, which together determine the tuning effect of quantum emission observed in experiments. To validate this framework, we fabricated both gradient and uniform Mie void arrays using focused ion beam (FIB) milling into amorphous silicon substrates. From an experimental perspective, we demonstrate that silicon-based dielectric Mie voids enable flexible modulation of quantum emission through geometric shaping, with gradient-array-induced emission showing excellent agreement with theoretical predictions. In uniform Mie void arrays, we observe accelerated radiative decay rates thanks to Mie resonances, and quantitatively validate a strong linear correlation between the model-predicted quantum emission tuning factor and the experimentally measured emission intensity. Building upon this analytical framework established in silicon Mie voids, we further design and realize a bimodal nanophotonic structure with single-void-per-pixel spatial resolution that displays distinct patterns under white-light microscopy (bright- and dark-fields) and photoluminescence micrograph. This work establishes a theoretical foundation for the effective tunability of quantum emission, experimentally validates the versatility and spatial programmability of all-dielectric Mie voids, and opens a new and adaptable platform for light-emitting devices, optical information modulation, encrypted displays, super-resolution fluorescence imaging and sensing^{21,42,52,54-58}.

Results

Mie resonators

The scattering response and multipoles decomposition of all-dielectric Mie resonators provide fundamental insights into their local field confinement and resonance coupling with quantum emitters^{6,51}. Silicon, owing to its high refractive index, low cost, and compatibility with scalable industrial nanofabrication techniques, stands out as a prime candidate for realizing Mie-type nanophotonics^{56,59-61}. To systematically evaluate its potential, we begin our analysis by considering the elementary case of two prototypical configurations in vacuum: an individual Mie particle and a single Mie void. The dielectric medium is assumed to be homogeneous and isotropic, with its optical constants (refractive index and extinction coefficient) provided in [Supplementary Section S1](#). The Mie particle is modeled as a solid silicon sphere with the quantum emitter positioned adjacent to its surface (Figure 1A). By contrast, the Mie void is represented by a hemispherical air cavity etched into silicon (Figure 1B), a geometry that is both experimentally feasible and optically accessible in the visible wavelength range, with the quantum emitter embedded within the void. The influence of the Mie resonator on quantum emitters can be analyzed from two complementary aspects⁵³: (i) the confinement of the local electromagnetic field at the excitation wavelength, and (ii) the resonant coupling between the quantum emitter and the multipoles of the Mie resonator at the emission wavelength. Both effects manifest respectively as excitation enhancement and quantum yield enhancement.

The near-field electromagnetic distributions and multipolar contributions are computed under linearly polarized plane wave illumination for both Mie resonators. As shown in Figure 1C, the incident electric field at the excitation wavelength is predominantly confined within the high-index dielectric of the Mie particle or strongly pinned near its surface¹³. This confinement indicates that the excitation enhancement rapidly diminishes as the quantum emitter moves just a few nanometers away from the particle⁵³. Furthermore, as shown in Figure 1D, the dominant multipolar components — extracted via multipoles expansion ([Supplementary Section S2](#)) — are also primarily located inside the silicon host⁶. This spatial separation precludes efficient resonant coupling with external quantum emitters placed more than ~ 20 nm away, thereby limiting the extent of emission control achievable in solid Mie resonators⁵³. In contrast, Figure 1E demonstrates that the Mie void resonators concentrate the incident electric field within the low-index air void, which is fully accessible for quantum emitters and minimizes energy loss inside the dielectric. As shown in Figure 1F, the emission multipolar modes of the

Mie void are also strongly localized within the air cavity^{5,19}, enabling effective resonant coupling with quantum emitters residing inside the void and thereby inducing a pronounced Purcell effect. Importantly, since the modal content in the void air is highly sensitive to its geometry, this configuration also offers an effective mechanism for spatially resolved emission tuning at the single-resonator level, independent of neighboring nanostructures. By tailoring the geometry of individual Mie voids, one can modulate the distinct resonant cavity modes confined within their own air regions, thereby enabling spatially independent control of quantum emitters residing inside each mode volume. This principle lays the physical foundation for ultrahigh-spatial-resolution quantum emission encoding patterns, free from cross-talk between adjacent pixelated voids, as will be illustrated in the final section of this work.

To further elucidate the optical resonances supported by the two Mie resonator systems, we performed a multipole analysis of their scattering cross sections, extracting the wavelength-resolved Mie scattering efficiency (see [Supplementary Section S3](#) for computational details). Figure 1G shows the multipoles decomposition for a 100 nm-radius silicon particle, while Figure 1H presents the results for a 430 nm-radius hemispherical Mie void. In the case of the solid Mie particle, a single dominant mode or, at most, two distinct resonances typically govern the scattering response at a specific wavelength. By contrast, the Mie void redistributes the modal energy over a broader spectral range, granting multiple modes concurrent access to the radiation channel, albeit with a lower overall scattering efficiency. Figures 1I and 1J further provide dimension- and wavelength-resolved Mie scattering efficiency maps for particle radii from 40 to 180 nm and void radii from 200 to 800 nm. These dimension sweeps are specifically selected to align the dominant multipoles with the operational bandwidth of visible-light quantum emitters. It is evident that the multipolar modes in both Mie resonators preserve similar modal identities and exhibit a correlated, approximately linear dispersion trend across feature sizes. Interestingly, a critical difference arises in the short-wavelength regime: for the Mie particle, the strongest-order modal scattering efficiencies — particularly those of the electric and magnetic quadrupoles — drop off rapidly and even vanish completely below ~ 450 nm. This degradation can be attributed to the substantial resonant absorption losses within the silicon material in this regime, as indicated by its extinction coefficient ([Supplementary Figure S1B](#)). In contrast, the Mie void configuration exhibits no such absorption-induced scattering suppression, reinforcing the conclusion that air-modes reduce optical losses and allow for robust modal persistence over a wide visible range.

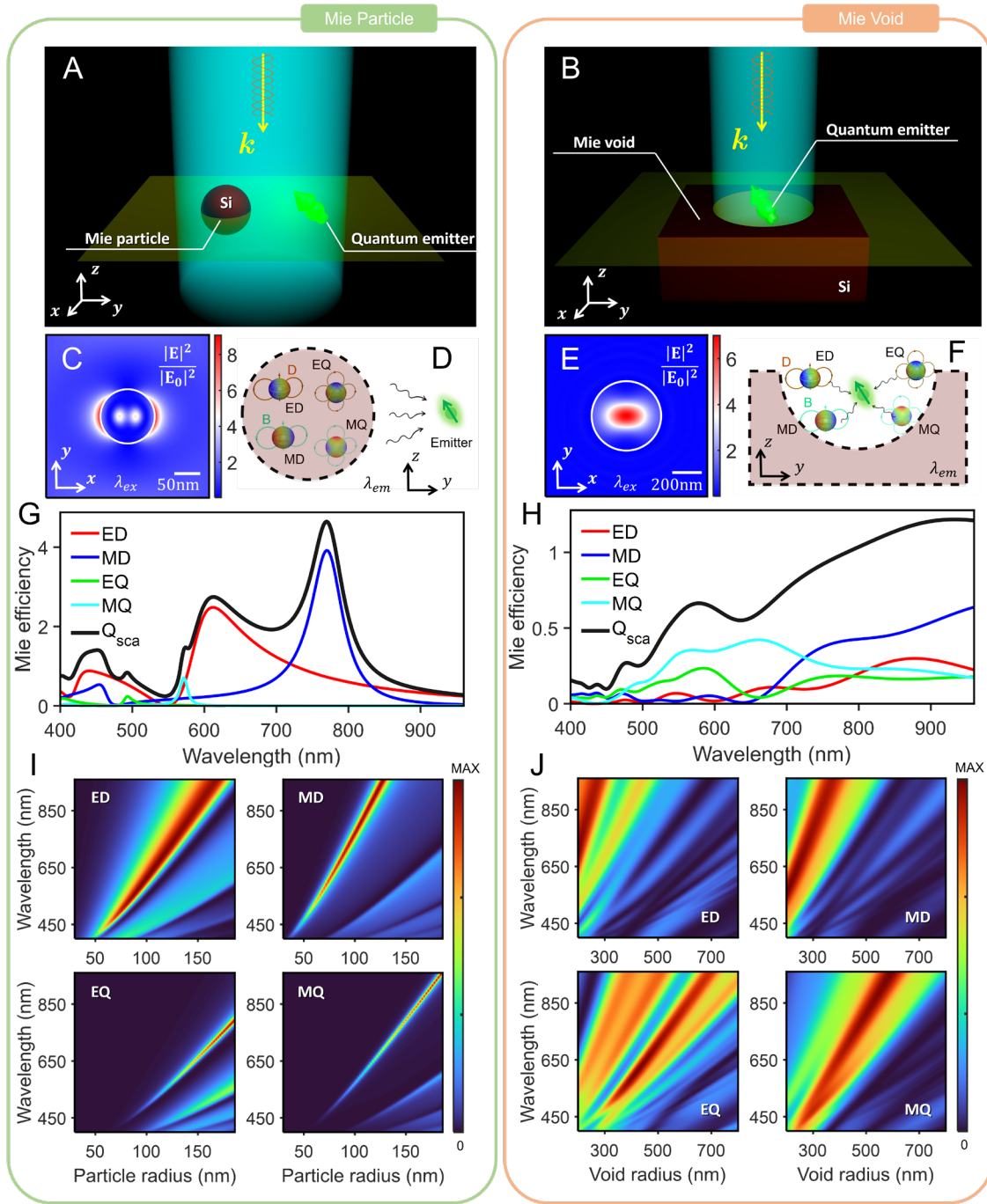


Fig. 1. Silicon-based Mie resonators reveal local field confinement and the multipole modes that couple to quantum emitters. (A) Schematic of a quantum emitter placed adjacent to a silicon Mie particle and illuminated by a plane wave. (B) Schematic of a quantum emitter embedded in a hemispherical Mie void etched into silicon under the same illumination. (C) Excitation enhancement and (D) quantum yield enhancement mechanisms are illustrated respectively for the Mie particle. They correspond to the near-field distribution at the excitation wavelength and the spatial distribution of multipolar modes at the emission wavelength. Most fields are confined within or pinned to the high-index dielectric, limiting external emitters

access and coupling. **(E)** and **(F)** show the corresponding plots for the Mie void, where both excitation fields and emission resonant modes are concentrated in the air void, allowing interior emitter access and enabling enhanced coupling with internal emitters. Note that in the schematic diagrams **(D)** and **(F)**, the electric dipole (ED), magnetic dipole (MD), electric quadrupole (EQ), and magnetic quadrupole (MQ) modes are shown separately for clarity, although in reality these multipolar modes coexist and spatially overlap. **(G)** Multipoles decomposition of the scattering efficiency for a 100 nm-radius particle and **(H)** for a 430 nm-radius void. **(I)** Wavelength- and size-resolved Mie scattering efficiency maps for Mie particles (radii: 40–180 nm) and **(J)** for Mie voids (radii: 200–800 nm).

Quantum emission tuning

To quantitatively investigate the quantum emission tuning capabilities of a dielectric–air nanophotonic environment, we consider a Mie void resonator etched into a high-index silicon substrate (Figure 2A). Under realistic fabrication conditions, such Mie voids typically exhibit a truncated conical profile characterized by a height h and upper/lower radii R_1 and R_2 . For analytical clarity and computational efficiency, we start by modeling the Mie void as a vertically symmetric cylindrical cavity with a quantum emitter placed at its geometric center. This configuration also supports strong Mie resonances that confine the field predominantly within the low-index air region and facilitates strong coupling with embedded dipolar quantum emitters. When illuminated by a normally incident plane wave polarized along the y -direction and propagating along z -direction, the quantum emitter undergoes optical excitation governed by the local electric field $\mathbf{E}_d(\mathbf{r}_0, \omega)$ at the emitter location. A detailed derivation of the excitation enhancement factor F_{ex} based on this field confinement is provided in [Supplementary Section S4](#). In practice, quantum emitters are typically distributed randomly and uniformly throughout the air-filled volume of the Mie void. The vertical electric field distributions, plotted in two orthogonal cross-sections (Figures 2B and 2C), show that the field is spatially localized within a portion of the void. To evaluate the overall excitation enhancement within the Mie void, we adopt a spatially averaged formulation of the enhancement factor,

$$\bar{F}_{ex}(\mathbf{r}_0, \omega) = \frac{1}{V} \int_V \frac{|\mathbf{E}_d(\mathbf{r}_0, \omega)|^2}{|\mathbf{E}_0(\mathbf{r}_0, \omega)|^2} dV, \quad (1)$$

where the integration volume V refers to the region encompassing the Mie void and an overlying layer of height t , which corresponds to the thickness of the emitter-containing

medium. In this study, t was set to be 565 nm, consistent with the thickness of the 10% PVA coating layer used in the subsequent experiments. The complex amplitude of the incident electric field at the location \mathbf{r}_0 of the emitter is $\mathbf{E}_0(\mathbf{r}_0, \omega)$ and ω is the angular frequency in free space. Building on the above framework, we numerically computed the near-field distributions for Mie voids across a broad range of geometric parameters, and subsequently evaluated their spatially averaged excitation enhancement factors \bar{F}_{ex} , as shown in Figure 2D. The small-radii Mie voids (below ~ 400 nm) exhibit a strong dependence of \bar{F}_{ex} on the cavity depth. $\bar{F}_{ex} < 1$ can even be observed for deep and narrow cavities, indicating that such void geometries fail to achieve effective field confinement therein. In such cases, the cavity geometry restricts the accessible excitation channels and thereby suppresses energy delivery to the emitter. By contrast, in large-radii Mie voids, the excitation enhancement factor becomes relatively insensitive to the void depth and plateaus near a value of ~ 1.5 . This behavior suggests that lateral confinement dominates the field enhancement mechanism in large-diameter cavities, and that the excitation enhancement becomes less sensitive to the vertical geometry once stable resonance conditions are satisfied, implying a geometric saturation of the local field confinement effect.

The preceding analysis focused solely on the excitation enhancement effect induced by the Mie void under optical illumination. However, a comprehensive understanding of quantum emission tuning requires also evaluating the resonator-mediated enhancement of spontaneous emission — namely, the Purcell effect. To isolate this contribution, we eliminate the external illumination and consider an emitter undergoing spontaneous decay into three channels (Figure 2A): intrinsic nonradiative decay ($\gamma_{nr,0}$), radiative emission to the far field (γ_{rad}), and additional absorption in the surrounding lossy dielectric (γ_{abs}). [Supplementary Section S5](#) provides a quantitative characterization of the resonant coupling and emission dynamics using three dimensionless factors: the Purcell factor (F_p), the far-field radiation factor (μ), and the dielectric absorption factor (μ_1). The energy-based definitions and integration methodologies for extracting these parameters from simulations are also detailed therein. The Purcell factor describes the total external modification of the emitter decay rate induced by changes in the optical LDOS, the dielectric absorption factor quantifies the portion of energy dissipated within the surrounding lossy dielectric medium, and the far-field radiation factor denotes the fraction of energy radiated to the far field and collected by a far-field receiver. The combined effect of these three terms governs the resonance-modified quantum yield enhancement factor F_q ,

$$F_q(\mathbf{r}_0, \omega) = \frac{q_d}{q_0} = \frac{F_p - \mu_1}{q_0(F_p - 1) + 1} = \frac{\mu}{q_0(F_p - 1) + 1}, \quad (2)$$

where q_0 and q_d are the intrinsic and resonance-modified quantum yields, respectively. This framework enables us to systematically evaluate the geometry modulation of the emitter-resonator interactions. Figure 2E presents calculations of a dipole emitter placed at a distance of 150 nm from the center of a 100 nm-diameter silicon Mie particle. We computed the Purcell factor, far-field radiation factor, and dielectric absorption factor for two orthogonal dipole orientations: one aligned vertically (left in Figure 2E) and the other horizontally across the particle center (right in Figure 2E). In both cases, the far-field receiver surface A is defined as a spherical shell enclosing the resonant system. The results confirm the energy-conservation relation $F_p = \mu + \mu_1$, thereby validating the reliability of the simulations and allowing for simplification in subsequent analyses. Specifically, this relation eliminates the need for full-volume absorption integration (P_{abs}) to determine μ_1 in Eq. 2, reducing the procedure to the computation of the surface-integrated radiated power (P_{rad}) for evaluating μ . Moreover, Figure 2E reveals a strong dependence of the quantum emission enhancement on emitter orientation, highlighting the anisotropic nature of the emitter-resonator coupling. This quantum yield enhancement equation also shows how resonant coupling in Mie resonators impacts quantum emitters with varying intrinsic quantum yields q_0 . Figure 2F shows the relationship between F_q and q_0 for different combinations of Purcell and dielectric absorption factors. When $F_p > 1$, indicating intrinsic resonant enhancement, the spontaneous emission improvement becomes more pronounced for emitters with lower intrinsic quantum yields⁶². In contrast, when $F_p < 1$, F_q remains consistently below unity, signifying actual emission suppression — an effect that is again more severe for emitters with lower q_0 . To achieve substantial emission enhancement ($F_q > 1$) through resonant coupling in dielectric Mie resonators, the dielectric absorption must be sufficiently low such that $\mu < (F_p - 1)(1 - q_0)$. Additional calculation results with strong Purcell effect and interaction between a quantum emitter and the nanophotonic resonator are provided in [Supplementary Section S6](#).

In practical experimental setups, far-field detectors are typically positioned above the Mie void structures. To reflect this configuration in the simulations, we define the far-field receiver surface A as an infinite horizontal plane located above the void. This setup is conceptually analogous to projecting the spherical receiver surface of a Mie particle onto a planar receiving surface (see inset of Figure 2D). We conducted a systematic sweep of the geometric parameters

of silicon Mie voids and computed the corresponding values of the Purcell factor, the far-field radiation factor, and the dielectric absorption factor, as summarized in Figures 2G, 2H, and 2I, respectively. Additional results with extended height variations can be found in [Supplementary Section S7](#). These results collectively reveal that the quantum yield enhancement in Mie voids arises from the superposition of resonant coupling between the embedded emitter and void-supported multipolar modes. Notably, the trends of these three factors as functions of the void radius closely resemble the radius-dependent behavior of multipolar Mie scattering efficiencies previously observed for Mie voids (Figure 1J). Since the far-field receiver plane *A* only accounts for upward radiation channels, the observable quantum yield enhancement factor is consistently less than unity. Nonetheless, resonance coupling remains the dominant mechanism by which Mie voids control the spontaneous emission behavior of quantum emitters embedded therein.

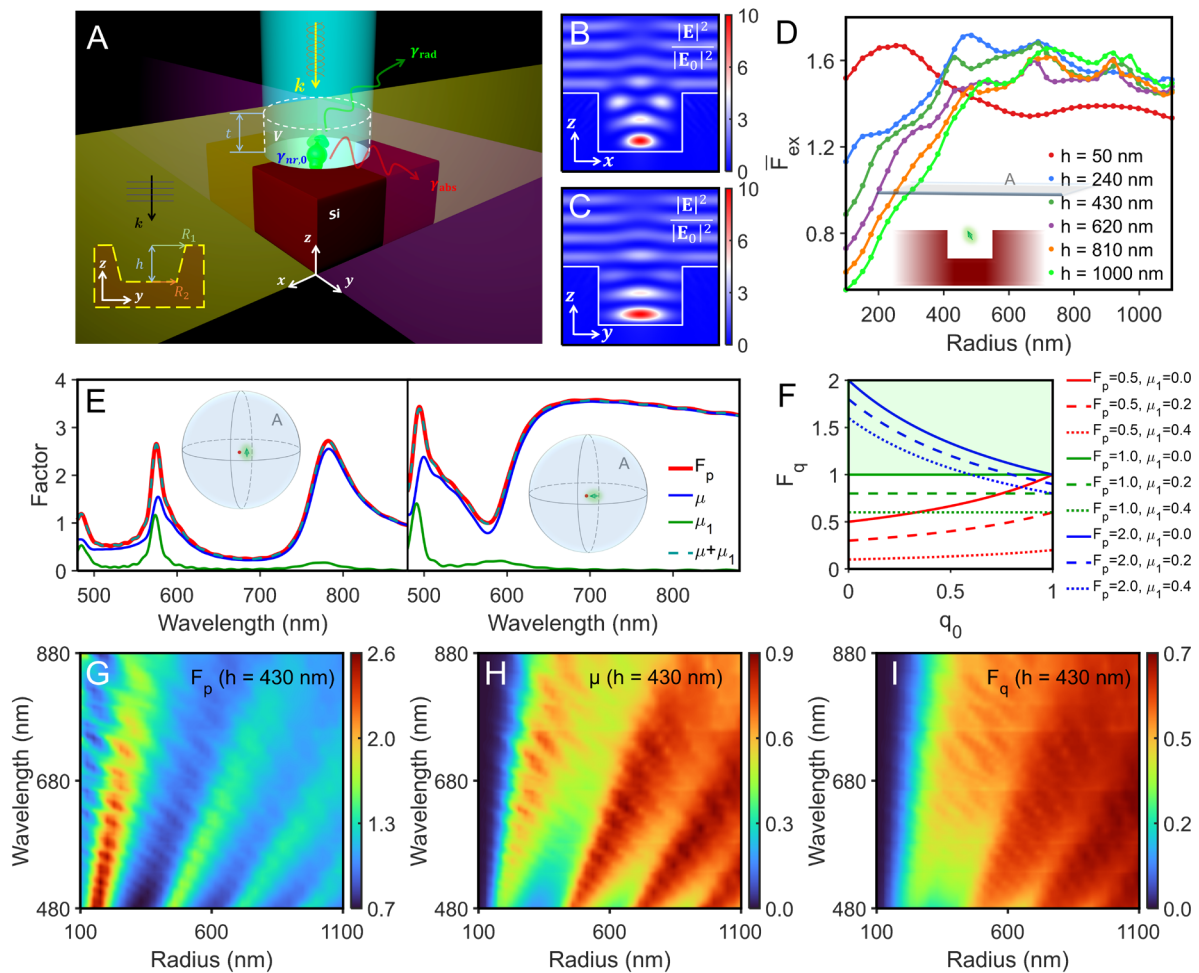


Fig. 2. Tuning quantum emission with all-dielectric Mie void resonators. **(A)** Schematic illustration of quantum emission processes in a silicon Mie void resonator. A quantum emitter

(e.g., a fluorophore or quantum dot) is embedded inside a Mie void. Under optical excitation from a normally incident y -polarized plane wave (blue beam, wavevector k), the emitter undergoes near-field excitation and subsequent spontaneous emission. Three decay rates (γ_{rad} , $\gamma_{\text{nr},0}$, γ_{abs}) determine the resonator-modified quantum yield. The inset shows a truncated conical geometry more representative of realistic fabricated Mie voids, characterized by height h and top/bottom radii R_1 and R_2 . **(B)** and **(C)** Cross-sectional electric field intensity distributions $|\mathbf{E}|^2/|\mathbf{E}_0|^2$ in the xz - and yz -planes, respectively, showing field confinement within the Mie void. **(D)** Spatially averaged excitation enhancement factor \bar{F}_{ex} as a function of the geometric parameters of cylindrical Mie voids. The inset illustrates the definition of the far-field receiver plane A positioned above the Mie void, used for radiative energy calculations. **(E)** Energy-conservation relation for a dipole emitter placed 150 nm from the center of a 100 nm-diameter silicon Mie particle. Left: vertical dipole orientation; Right: horizontal dipole orientation. Shown are the Purcell factor (F_p), far-field radiation factor (μ), dielectric absorption factor (μ_1), and their sum, validating the relation $F_p = \mu + \mu_1$. Insets indicate the spherical receiver surface A enclosing the particle–emitter system. **(F)** Dependence of the resonance-modified quantum yield enhancement factor F_q on the intrinsic quantum yield for selected values of F_p and μ_1 , as described by Eq. 2. The enhancement is strongly dependent on q_0 , with low- q_0 emitters being influenced more by resonance coupling. **(G)** Parameter sweeps of Purcell factor, **(H)** far-field radiation factor, and **(I)** quantum yield enhancement factor as functions of void radius and emission wavelength, with void depth fixed at 430 nm. The far-field collection is restricted to upward emission.

Experimental Results

We fabricated a gradient array of Mie-void resonators in amorphous silicon using FIB milling to experimentally validate the capability of Mie voids to modulate the quantum emitters behavior. The gradient array refers to a two-dimensional layout in which the milling radius of the Mie voids increases linearly along the horizontal (row) direction, while the milling depth increases linearly along the vertical (column) direction. Figure 3A presents scanning electron microscope (SEM) images of the fabricated sample: the central panel shows a top-down view of the full array, while the four corner insets display oblique-angle SEM images taken at a 32° tilt, providing clear visualization of the gradual variations in both radius and depth of the cylindrical Mie voids across orthogonal directions. To precisely characterize the geometrical profile of the fabricated voids, we further performed atomic force microscopy (AFM)

characterization of the array ([Supplementary Section S10](#)). In fact, the fabricated voids exhibit truncated conical geometries; for consistency with numerical modeling, their effective radius is defined as the average of the top and bottom radii. The measured radii vary from 160 nm (leftmost column) to 360 nm (rightmost column), and the depth increases from 30 nm (bottom row) to 770 nm (top row). Figures 3B and 3C show the bright-field and dark-field optical microscope images of the pristine Mie-void gradient array, respectively. While similar reflectance results have been reported in Ref. 19, we reproduce them here to establish a comprehensive foundation for studying quantum emission, and to adopt bright-field reflection imaging as one of the display modalities in the following sections. These images reveal that air-defined Mie voids support geometry-dependent reflected and scattered colors, with spatially varying reflection and scattering spectra clearly discernible across the array. Notably, even two Mie-void pixels that exhibit markedly different spectral features in the bright-field image can appear similarly colored under dark-field observation conditions. This phenomenon offers additional flexibility in designing subwavelength-encoded patterns with ultrahigh spatial resolution, enabling multiple distinct spectral responses to be encoded within a single nanophotonic pixel.

In the further experiments, a 10% polyvinyl alcohol (PVA) solution is employed as the host matrix for the quantum emitters and spin-coated onto the surface of the Mie-void gradient array, forming a conformal PVA-coating layer of uniform thickness (Figure 3D). The thickness and refractive index of this PVA film were characterized using spectroscopic ellipsometry, with detailed results provided in [Supplementary Section S1](#). Since the refractive index of 10% PVA is also much lower than that of amorphous silicon⁶³, the coated voids can effectively retain the similar characteristics of dielectric–air Mie resonators, however, as will be shown later, their resonant spectral positions experience noticeable shifts due to the change of the refractive index in the void. In this experiment, we chose fluorescein isothiocyanate (FITC) molecules as representative quantum emitter. These emitters are uniformly dispersed and randomly oriented throughout both the Mie voids and the overlying PVA-coating layer. For simulation, this distribution is modeled as a dipole cloud comprising an ensemble of randomly oriented dipoles distributed throughout the molecule-filled volume (Figure 3E). The collective emission of this dipole cloud within a single Mie void can be characterized by the averaged resonance-modified quantum yield enhancement factor \bar{F}_q , expressed in Eq. 3. This averaging procedure involves not only spatial integration over the emitter volume, but also spectral wavelength integration

across the emission bandwidth and angular integration over all possible dipole orientations in 4π steradians,

$$\bar{F}_q = \frac{1}{4\pi V \Delta\lambda} \int_V dV \int_{\lambda_0}^{\lambda_0 + \Delta\lambda} d\lambda \int_0^{2\pi} d\phi \int_0^\pi \frac{q_a}{q_0} \sin \theta \, d\theta, \quad (3)$$

where, the integration limit λ_0 to $\lambda_0 + \Delta\lambda$ corresponds to the full width at half maximum (FWHM) of the quantum emitter spectrum, which for FITC emission spans 510 nm – 540 nm. The angles ϕ and θ represent the two orthogonal angular components (the azimuthal and polar angles) defining the dipole orientation in three-dimensional space. Figures 3F and 3G show the bright-field and dark-field optical microscope images, respectively, of the Mie void gradient array after PVA coating. Compared to their counterparts in air, the resonant color of each void indicates a systematic shift of the resonant wavelength.

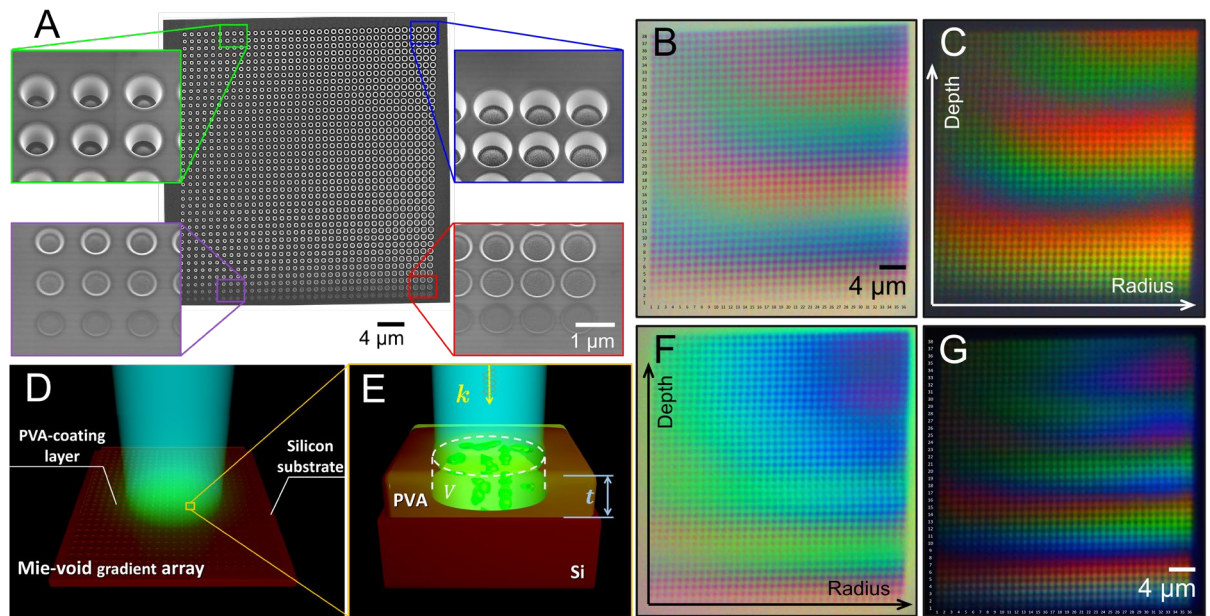


Fig. 3. Gradient array of silicon Mie voids without and with PVA coating. (A) SEM images of the fabricated Mie-void gradient array. The central panel shows a top-down view of the entire array, with four corner insets displaying 32°-tilted SEM views of representative voids to reveal their depth profiles. The array is patterned on a square lattice with a periodicity of 1200 nm. The nanovoid depth varies from 30 nm to 770 nm across 38 rows, and the radius varies from 160 nm to 360 nm across 36 columns. (B) Bright-field and (C) dark-field optical microscope images of the gradient array. The Mie voids exhibit distinct reflectance and scattering spectral resonances that vary across the array, as indicated by the color variations observed for both imaging modes. (D) Schematic of the array sample spin-coated with a transparent PVA

(10% w/v) thin film uniformly embedding quantum emitters and (E) magnified view of a single Mie void within the PVA-coating layer, showing a volumetric distribution of randomly oriented quantum emitters extending from the void base to the film surface. (F) Bright-field and (G) dark-field optical microscope images after applying the PVA coating. The introduction of the low-index PVA layer causes a small but measurable shift in the resonance spectra of the Mie voids due to the modified local photonic environment in both imaging modes.

Next, we characterized the quantum emission tuning effect in the gradient array sample using spatially resolved spectroscopy and time-correlated single-photon counting (TCSPC). The schematic of the optical setup is illustrated in Figure 4A (with the detailed physical setup and components provided in [Supplementary Section S9](#)). A 488 nm pulsed laser was employed to excite the FITC fluorophores, and the emitted fluorescence was collected using both a spectrograph and a single-photon counting detector, enabling measurements of emission spectra, fluorescence lifetimes, and spatially resolved quantum emission maps (see [Materials and Methods](#) for details). We numerically evaluated the spatially averaged excitation enhancement factor, \bar{F}_{ex} , of PVA-coated Mie voids with varying radius and depth according to Eq. 1, using a PVA layer thickness of 565 nm, identical to that in the experiments. For reference, we also calculated $\bar{F}_{ex,b}$, the corresponding excitation enhancement factor in the PVA layer on a bare silicon substrate. Figure 4B presents the resulting relative excitation enhancement $\bar{F}_{ex}/\bar{F}_{ex,b}$ for each combination of Mie void dimensions, comparing the enhancement achieved within the structured void to that on a bare silicon surface coated with the same PVA layer. In an analogous manner, we computed the resonance-modified quantum yield enhancement factor \bar{F}_q for quantum emitters embedded in the PVA-coated Mie voids of different sizes using Eq. 3, and compared it to the corresponding value $\bar{F}_{q,b}$ for emitters uniformly distributed in the PVA layer on the bare substrate. The resulting relative quantum yield enhancement $\bar{F}_q/\bar{F}_{q,b}$ is presented in Figure 4C. These results highlight the two distinct and independent mechanisms by which a Mie void tunes quantum emission: (1) enhancement of local excitation field and (2) modification of spontaneous emission via resonant coupling. Both effects are essential contributors to the overall tuning effect of quantum emission and the combined quantum emission tuning factor F_{qe} can be expressed as⁵³:

$$F_{qe}(\mathbf{r}_0, \omega) = F_{ex}(\mathbf{r}_0, \omega) \cdot F_q(\mathbf{r}_0, \omega). \quad (4)$$

By taking the ratio between the Mie void configuration and the unstructured bare silicon substrate, the spatially averaged relative form $\bar{F}_{qe}/\bar{F}_{qe,b}$ is obtained, as visualized in Figure 4D. This theoretical prediction is directly compared to the experimentally acquired quantum emission map shown in Figure 4E. The white dashed box in Figure 4D outlines the experimentally accessed range of void geometries (radius and depth, [Supplementary Section S10](#)), which corresponds to the region measured in Figure 4E. The comparison reveals strong agreement in the spatial distribution of emission intensity, confirming the efficacy of the combined excitation and emission enhancement framework. Notably, compared to quantum emitters situated on the bare silicon surface, the Mie-void configuration yields a maximum emission enhancement ratio of 2.6 and a minimum suppression ratio of 0.5, whereas the experimentally observed range of variation is narrower (approximately 0.9 – 2.5). These discrepancies are primarily attributed to fabrication imperfections and measurement uncertainties. In particular, the FIB process produces truncated conical void profiles rather than ideal cylindrical geometries (as illustrated in the inset of Figure 2A and [Supplementary Figure S13](#)), with deviations becoming especially pronounced for deep and narrow voids. Additional fabrication-induced factors — such as surface roughness, edge rounding, and contamination with gallium — further affect the optical confinement and emitter-resonator coupling. On the measurement side, ensuring conformal thickness of the PVA coating and maintaining consistency between the excitation laser spot size and the Mie void aperture are critical for minimizing deviations between experimental results and theoretical predictions.

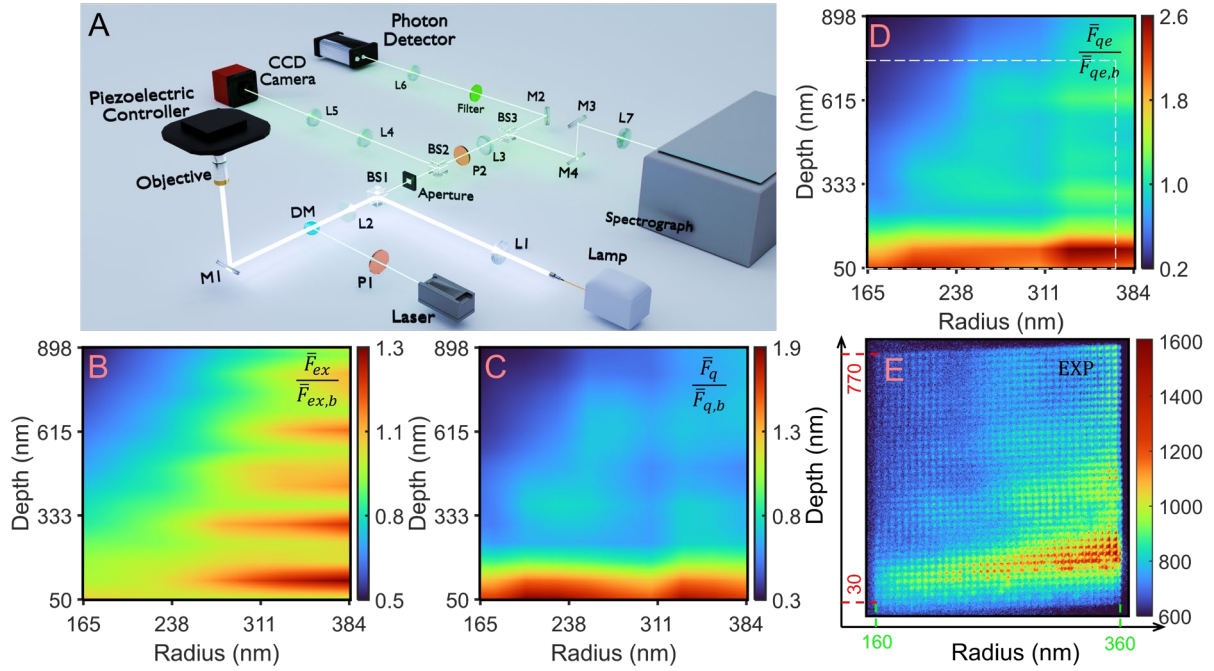


Fig. 4. Theoretical prediction and experimental measurements of quantum emission tuning with Mie void gradient arrays. (A) Schematic of the optical setup used for spectroscopic and TCSPC characterization. A 488 nm pulsed laser is synchronized with a time-resolved single-photon detector, and a digital piezoelectric positioning stage enables spatially resolved scanning of the sample. **(B–D)** Numerical simulations and calculations of the relative enhancement factors for cylindrical Mie voids with varying radius and depth, compared to a bare silicon substrate: **(B)** Relative excitation enhancement factor $\bar{F}_{ex}/\bar{F}_{ex,b}$; **(C)** Relative quantum yield enhancement factor $\bar{F}_q/\bar{F}_{q,b}$; **(D)** Combined relative quantum emission tuning factor $\bar{F}_{qe}/\bar{F}_{qe,b}$, computed using Eq. 4. **(E)** Experimental photoluminescence micrograph obtained by scanning the Mie void gradient array. Quantum emitters embedded within the PVA coating layer emit photons under pulsed excitation, and the resulting photon counts are spatially resolved. The region outlined by the white dashed box in **(D)** indicates the range of void geometries sampled in the experimental scan shown here.

Further, we fabricated a series of uniform Mie void arrays and experimentally characterized their optical response, including reflection spectra, resonance-tuned emission spectra, and the spontaneous emission lifetimes of embedded quantum emitters. As shown in Figure 5A, sample S_0 serves as a bare silicon reference without any nanostructures, and samples S_1 to S_5 are periodic arrays, each composed of 11 rows and 10 columns of identical Mie voids. While the

layout remains constant, the geometrical parameters of the voids vary across the different samples, enabling controlled tuning of the resonant properties. The reflection spectra for all five structured arrays are shown in Figure 5B. The observed spectral responses arise from the collective contributions of the uniform arrays, which in turn originates from the individual resonant characteristics of each void. Similarly, the photophysical properties observed from quantum emitters within the arrays reflect the cumulative effect of resonant tuning at the single-void level. After spin-coating the arrays with a PVA layer uniformly embedded with quantum emitters, we measured the fluorescence emission spectra as shown in Figure 5C. Across all geometries, the Mie voids exhibit appreciable broadband resonance-enhanced emission. Although Mie resonances yield lower enhancement factors compared to high-Q resonances such as Fano resonances or BICs^{41,43,64}, their broad resonant bandwidth enables robust spectral conformity, preserving the overall intrinsic emission profile of quantum emitters and facilitating conformal enhancement across a wide wavelength range. Time-resolved TCSPC measurements were performed to evaluate the spontaneous emission lifetimes of quantum emitters in different Mie voids. As shown in Figure 5D, the emission decay of the emitters on the bare silicon surface (S_0) were fitted using a single-exponential decay model based on the natural exponential form, yielding a baseline radiative decay lifetime of $\tau_0 = 2.68$ ns. In contrast, quantum emitters on structured region displayed accelerated decay dynamics and systematically shortened lifetimes, implying enlarged spontaneous emission rates thanks to resonator-mediated coupling. For rigorous analysis, the TCSPC data sampled from the uniform arrays were fitted using a bi-exponential decay model to account for contributions from emitters located both within and outside the voids ([Supplementary Section S11](#)). Each fitted radiative decay curve includes a common longer component close to τ_0 , attributed to emitters residing in non-Mie-resonant regions outside the voids. The shortened lifetime component, which varies with the void geometry — for example, $\tau_1 = 1.04$ ns for the quantum emitters on array sample S_1 — reflects the Purcell-enhanced decay channels introduced by the Mie voids. This tunable reduction in emission lifetime demonstrates the feasibility of geometrically engineered Mie voids for continuous and precise control over radiative decay dynamics. Finally, the total emission intensity I for each sample was obtained by integrating the corresponding fluorescence spectrum shown in Figure 5C. The relative enhancement was evaluated by normalizing to the bare substrate reference, defined as I/I_b , where I_b represents the integrated emission intensity from quantum emitters on the unstructured silicon surface. The experimental intensity enhancement ratios I/I_b were plotted against the theoretical predictions $\bar{F}_{qe}/\bar{F}_{qe,b}$, as

presented in Figure 5E. While the experimental data points (fitted by the blue dashed proportional line) from the uniform Mie void arrays follow the overall trend predicted by the theoretical model, they consistently fall below the ideal unity-slope line (red dashed line), by typically 5.4%. This modest deviation arises primarily from the presence of non-void regions within each periodic array, which contribute untuned baseline emission, as well as from experimental measurement uncertainties. Moreover, the depth of the Mie voids not only governs the resonance-mediated tuning of quantum emission but also affects the overall fluorescence collection efficiency, introducing further deviations between experimental observations and modeled results.

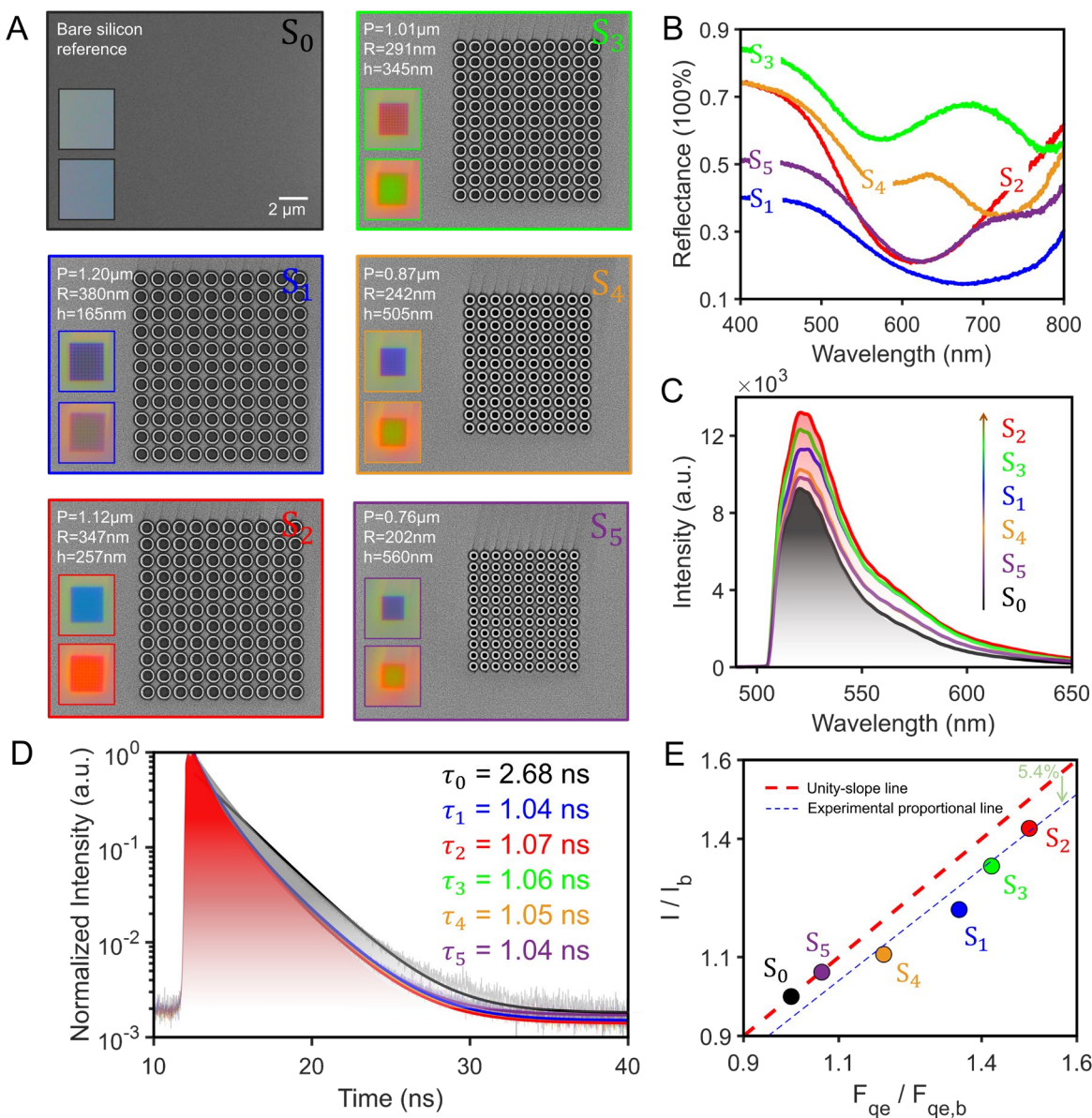


Fig. 5. Quantum emission measurement and characterization of uniform Mie void arrays.
(A) Scanning electron micrograph (right) and optical microscope images (top left: without PVA

coating; bottom left: with PVA coating) of fabricated uniform Mie void arrays. All SEM images share the same scale bar. Sample S_0 serves as the bare silicon reference, while S_1 - S_5 correspond to periodic arrays of cylindrical Mie voids, each comprising a 11×10 grid with identical void dimensions. The arrays differ in void radius (R) and depth (h), while P denotes the array period. **(B)** Measured reflectance spectra of the uncoated uniform Mie void arrays. Color labels correspond to samples S_1 - S_5 . **(C)** Fluorescence emission spectra of the same arrays after spin-coating a PVA layer uniformly doped with quantum emitters. Each Mie void geometry exhibits enhanced emission relative to the bare substrate, and the resonance-enhanced emission retains spectral conformity across the emission bandwidth. **(D)** TCSPC measurements comparing the decay dynamics of emitters on the bare silicon surface (black, fitted with a single exponential function) and within the Mie void arrays (others, fitted using bi-exponential decay functions). The faster decay components reflect Purcell-enhanced spontaneous emission governed by Mie resonances. **(E)** Regression between theoretical and experimental quantum emission enhancement ratios. Experimental values are obtained by integrating the emission spectra in **(C)** and normalizing to S_0 . The red dashed line indicates the ideal unity-slope correlation.

Ultrahigh-Resolution Quantum Emission Encoding Pattern

Based on the preceding analytical model for tuning quantum emission via Mie voids, along with their characteristic reflection and scattering spectral shifts under bright- and dark-field illuminations, we designed a bimodal nanophotonic structure that encodes two high-resolution patterns⁶⁵, as illustrated in Figure 6. In this design, it displays the EPFL logo under bright-field optical microscopy, while the SJTU logo remains hidden and only emerges under either dark-field microscopy images or photoluminescence micrographs obtained from TCSPC scans. The spatial resolution of this pattern approaches the optical diffraction limit⁶⁶, with each pixel corresponding to a single Mie void with a submicron footprint. The pixel-level encoding scheme and geometric design of the Mie voids are illustrated in Figure 6A, where each void is assigned a two-bit binary code defining its optical response state. The first (least significant) bit determines the brightness state in the bright-field image — '1' for bright and '0' for dark — while the second (most significant) bit governs the brightness in both the dark-field image and the photoluminescence micrograph. For instance, a pixel with the binary state '10' corresponds to a cylindrical Mie void designed with a diameter of 770 nm and a depth of 418 nm. This configuration appears as a dark pixel in the bright-field image but as a bright pixel under both

dark-field and quantum emission channels. The dimensions for the four states ‘00’, ‘01’, ‘10’ and ‘11’ are indicated in Figure 6A. Following this binary encoding strategy, the high-resolution nanophotonic pattern was fabricated via FIB milling, with tilted-view and top-view SEM images shown in Figures 6A and 6B, respectively.

We next characterized the fabricated patterns using optical microscopy under white-light illumination to assess their encoded optical responses. For reference, the optical responses of the four elementary Mie-void states — including reflected visible intensity, scattered visible intensity, and the quantum emission tuning factor — were simulated, and the corresponding pixelated encoding patterns (Figures 6C, Figures 6D and Figures 6E) were compared with the experimental observations. Although subtle chromatic variations appear among the dark pixels in the experimental bright-field image of the uncoated pattern ([Supplementary Figure S15A](#)), grayscale conversion visually homogenizes the reflectance intensity of the dark-state pixels (Figure 6F), thereby rendering a clearly defined EPFL logo in the bright-field channel, in close agreement with the simulated result (Figure 6C). In contrast, the dark-field image of the uncoated sample (Figure 6G) reveals bright pixels with strong contrast against dark pixels, clearly forming the SJTU logo, consistent with the simulation (Figure 6D). For comparison, [Supplementary Section S12](#) presents additional ghost images with visual artifacts that arise when channels not explicitly engineered for independent image output are inadvertently activated. Moreover, quantum emission mapping of the coated sample produces a high-contrast image (Figure 6H), in which the SJTU logo emerges as bright pixels against a dark background, in agreement with the simulation (Figure 6E), thereby demonstrating selective and pixelated tuning of quantum emission by the Mie voids. This demonstration of ultracompact encoded patterns highlights the potential of Mie voids for spatially precise and spectrally selective control over optical reflectance, scattering, and quantum emission. By integrating this resonator-enabled quantum modulation mechanism with nanophotonic patterning, our approach achieves near-physical-limit resolution and enables multi-channel displays with independently programmable responses across bright-field, dark-field, and quantum emission modalities. This capability establishes a new paradigm for high-density, high-fidelity optical information encoding and encryption, paving the way for next-generation applications in quantum metasurfaces, secure nanoscale tagging, and multiplexed quantum photonic displays.

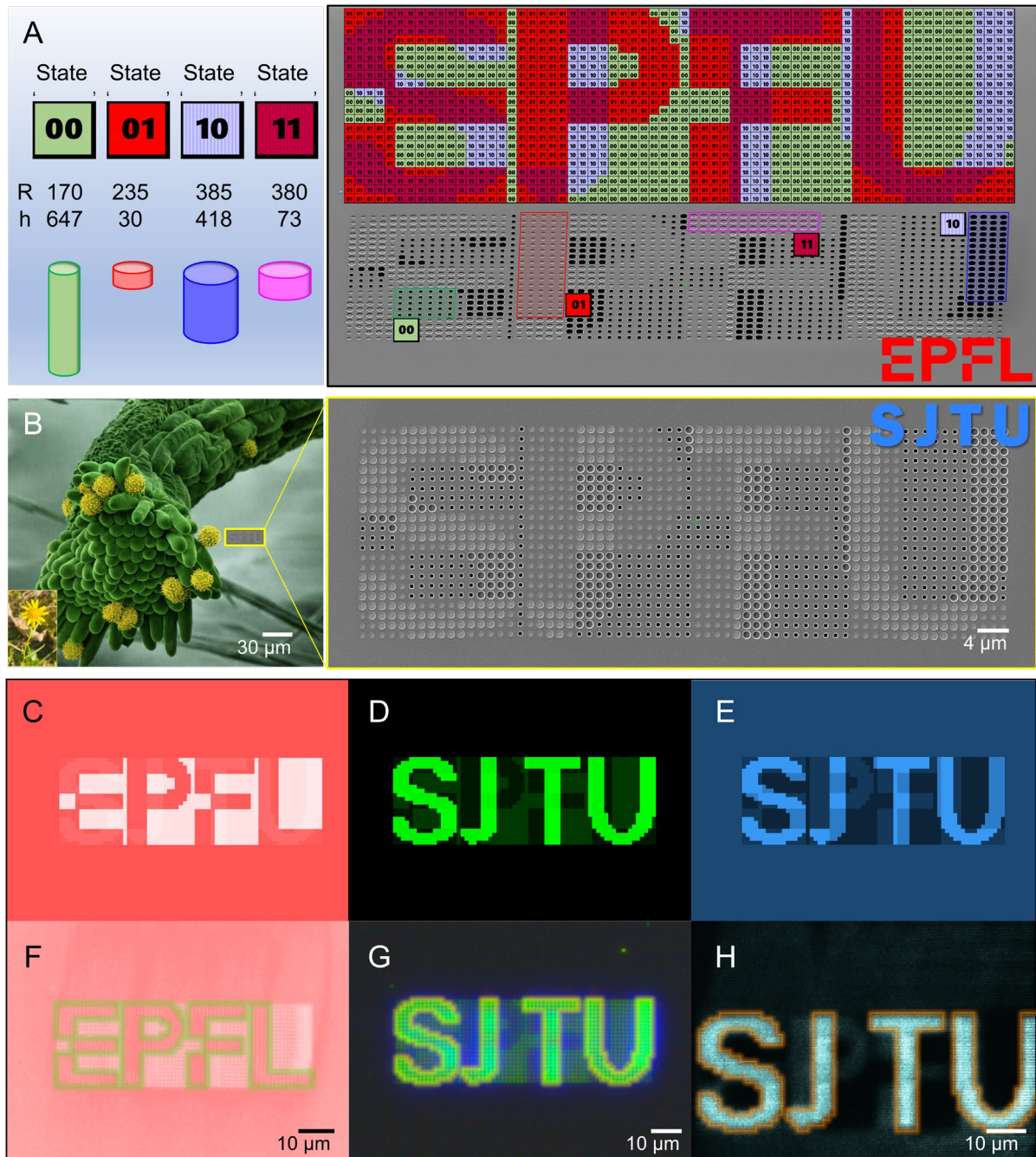


Fig. 6. Ultrahigh-resolution quantum emission encoding pattern displaying EPFL and SJTU logos. (A) Binary encoding scheme and geometric design of individual pixelated Mie void. Each state is assigned a two-bit code (00–11), with the corresponding radius (R) and depth (h) indicated below. The right panel shows the complete layout of the encoded pattern along with a tilted-view SEM image of the FIB-fabricated sample. **(B)** Top-view SEM image of the encoded pattern sample. For an intuitive sense of scale, the entire pattern is juxtaposed with a dandelion stamen in the SEM, revealing an overall footprint comparable to that of a single pollen grain. The right panels of **(A)** and **(B)** share the same scale bar. **(C–E)** Simulated

pixelated encoding patterns for **(C)** bright-field, **(D)** dark-field, and **(E)** quantum emission channels. **(F)** Experimental bright-field image of the uncoated sample, clearly revealing the EPFL logo. **(G)** Experimental dark-field image of the uncoated sample, directly rendering the SJTU logo. **(H)** Experimental photoluminescence micrograph of the coated sample, showing a high-contrast SJTU logo defined by emission enhancement at selectively encoded Mie void pixels.

Discussion

Freely and precisely engineering quantum emission underpins the development of light-emitting devices, super-resolution imaging and nano sensing, and quantum information technologies. However, achieving simultaneous and flexible control over local excitation enhancement and radiative quantum-yield modulation within an individual nanostructure remains challenging for conventional dielectric resonators, whose optical modes are predominantly confined within high-index media. In this work, we demonstrate air-defined silicon Mie voids as a flexible platform that grants quantum emitters direct access to dielectric resonance modes, enabling tunable quantum emission through the synergistic enhancement of localized excitation fields and resonance-mediated radiative decay. This behavior is quantitatively captured by an analytical framework that decouples and then unifies excitation and quantum-yield enhancement into predictive metrics. Through full-wave simulations and experiments on both gradient and uniform arrays, we observe Purcell-assisted lifetime shortening, geometry-dependent emission orchestrating, and a near-linear correlation between the model-predicted tuning factor and measured fluorescence intensities. Building upon this experimentally validated model, we realize a bimodal nanophotonic pattern with near-diffraction-limit pixel resolution, in which each subwavelength Mie void encodes the EPFL logo in bright-field images and the SJTU logo in dark-field and TCSPC-based quantum-emission maps — achieving spatially independent, multichannel control without inter-pixel crosstalk. Compared with solid Mie particles, the complementary void geometry relocates modal energy into air, suppresses absorptive losses, and strengthens emitter-mode coupling, thereby enabling spatially programmable and spectrally selective control at the single-resonator level. Beyond establishing a general methodology for the design of emitter-resonator architectures, these findings open new routes toward on-chip platforms for encrypted optical displays, super-resolution fluorescence imaging and sensing, compact nanoscale tagging, and multiplexed quantum photonic functionalities.

Materials and Methods

Fabrication

To realize the arrays of cylindrical Mie voids with independently varied depths and diameters on a silicon substrate, we employed focused ion beam (FIB) milling to directly fabricate each nanovoid individually. Prior to nanostructuring, the silicon chips were subjected to Piranha cleaning to remove organic contaminants and particulates generated during wafer dicing. The Piranha cleaning protocol involved two identical and successive baths of concentrated sulfuric acid (H_2SO_4 , 96%) heated at 100 °C and activated by hydrogen peroxide (H_2O_2 , 30%). All nanostructuring was performed using a Zeiss CrossBeam 540 dual-beam system, which combines gallium ion beam and electron beam columns for high-resolution nanofabrication and imaging. This tool enables FIB patterning with a nominal resolution less than 3 nm. The void depth was precisely controlled by adjusting the ion exposure dose. A base dose of $1 \text{ nC}/\mu\text{m}^2$ was defined, and a calibrated dose–depth relationship was experimentally established, revealing a near-linear correlation. The exposure dose for Mie voids was varied between 0.11 and 2.52 times the base dose, resulting in void depths ranging from 30 nm to 770 nm. All fabrication parameters for the nanovoid arrays—including spatial coordinates, diameters, and dose-adjusted depths—were generated via custom MATLAB R2024b scripts that output the complete milling instruction table. FIB milling was carried out in line-by-line mode, with circular geometries exposed in a concentric outward pattern mode, using a 30 kV acceleration voltage (EHT) and a beam current of 100 pA.

Characterization and Imaging

The microscale reflectance spectra of the periodic Mie void arrays were characterized using a custom-built inverted microscope system (Olympus IX73), equipped with a $20 \times$ objective lens (numerical aperture = 0.30), and a spectrograph (Andor SR-303i-A) integrated with a Newton 971 EMCCD camera. The EMCCD camera provides real-time spatial imaging of the sample surface, allowing precise alignment and definition of the regions of interest on the sample surface for spectral acquisition. Broadband illumination was provided by a high-power supercontinuum white light fiber laser (SuperK FIANIUM, NKT Photonics), which was focused onto the nanostructured region via the objective. The reflected signal was collected through the same objective and directed into the spectrograph for wavelength dispersion and spectral recording. Reflectance spectra were obtained by normalizing the measured reflection from the structured sample to that of the unstructured bare silicon substrate. Bright-field and dark-field optical microscope images of the gradient array sample and encoded nanophotonic pattern were acquired using a Nikon Optiphot 200 inspection microscope equipped with a $20 \times$, 0.40 NA objective lens. Illumination was provided by a halogen white light source, and the reflected light passed through a beam splitter before being captured by a CCD camera (Digital Sight DS-2Mv, Nikon). All optical images were processed solely by applying white balance correction taken from the bare silicon substrate, and no additional digital enhancement or filtering was applied.

The structural morphology of the Mie void arrays was characterized using field emission scanning electron microscopes (FE-SEM), including the Zeiss Crossbeam 550 (Carl Zeiss Jena GmbH) and Zeiss CrossBeam 540 systems, operated at an accelerating voltage (EHT) of 3.00 kV, beam current of 100 pA, and a working distance of 4.5 mm. High-resolution surface topography and void geometry were further characterized using atomic force microscopy (AFM;

Bruker FastScan, equipped with a 5 MP digital camera), which provided scanning probe imaging with a spatial resolution on the order of ångströms (Å), enabling precise quantification of individual void diameters and depths. Quantitative measurements of the void diameters and depths were performed and extracted by NanoScope Analysis software (version 1.50).

Quantum emission and lifetime measurement

The acquisition of quantum emission spectra and the measurement of emitter lifetimes were carried out using a custom-built experimental setup, as illustrated in Figure 2A. The lifetime measurements employed the time-correlated single-photon counting (TCSPC) method. An objective lens with $50 \times$ magnification (NA = 0.9) was used. A slit was placed at the image plane of the tube lens (L2) to restrict the collected light to the region of interest. A beam splitter (BS2) diverted part of the signal to a Thorlabs CCD camera, with two additional lenses (L4 and L5) positioned in front of the camera to provide image magnification. White-light illumination was used to visualize the sample on the camera and was switched off during spectrum and lifetime measurements.

FITC (fluorescein isothiocyanate dissolved in dimethyl sulfoxide, 30 $\mu\text{mol/L}$ embedded in 10% PVA) emitters were excited by a high-repetition-rate laser (LDH-D-C-488, peak wavelength: 488 nm), which was reflected by a dichroic mirror (DM) with a 500 nm cut-off wavelength. The resulting fluorescence emission, collected by the objective and peaking at \sim 517 nm, passed through the dichroic mirror since its wavelength exceeded the cut-off. To suppress laser sidebands, a polarizer (P2) was placed orthogonal to the laser polarization, which was defined by polarizer P1. The light was then focused by the lens pair L3 and L7 onto the input slit of an Andor spectrograph, enabling precise emission spectrum measurements.

Emitter lifetime measurements were performed using a TCSPC system (PicoHarp300, PicoQuant GmbH), controlled via SymPhoTime64 software. The 488 nm pulsed laser was synchronized with a time-resolved single-photon detector. A digital piezoelectric stage enabled emission mapping by recording photon counts at each point within a maximum scan range and depth of \sim 80 μm . Any point within the scanned region could be subsequently selected for lifetime acquisition. The lens pair L3 and L6 focused the collected light onto a single-photon avalanche diode (SPAD). Since the detector's active area was extremely small (\sim 50 μm), lens L6 was chosen to have a short focal length of 30 mm to achieve a tightly focused spot. A 520 nm bandpass filter (10 nm bandwidth) was used to isolate the fluorescence spectrum near the emission maximum. The measured decay curves were fitted with an exponential decay model to extract the emitter lifetimes.

Numerical Simulation

Geometric parameter sweeps of the Mie voids, including calculations of the near-field electromagnetic distributions, cavity mode volumes, quality factors, far-field radiation energies, and reflection spectra, were conducted using the finite-difference time-domain (FDTD) method implemented in commercial electromagnetic simulation software (FDTD Solutions, Ansys Lumerical 2023 R1, Canada). The spatial integration of the near field, calculation of the Purcell factor, far-field radiation factor, and dielectric absorption factor were performed using custom MATLAB scripts, based on the numerical near-field data and analytically defined expressions. The refractive indices and extinction coefficients of silicon substrate and the 10% PVA coating

layer used in the FDTD models were experimentally determined by spectroscopic ellipsometry (J.A. Woollam RC2) and fitted with empirical dispersion models.

References

- 1 Aigner, A. *et al.* Plasmonic bound states in the continuum to tailor light-matter coupling. *Science Advances* **8**, eadd4816, doi:doi:10.1126/sciadv.add4816 (2022).
- 2 Koshelev, K. *et al.* Subwavelength dielectric resonators for nonlinear nanophotonics. *Science* **367**, 288-292, doi:doi:10.1126/science.aaaz3985 (2020).
- 3 Maring, N. *et al.* A versatile single-photon-based quantum computing platform. *Nature Photonics* **18**, 603-609, doi:10.1038/s41566-024-01403-4 (2024).
- 4 Fu, Y., Jacobs, D. & Tan, S. Enhancing sensitivity in fluorescence measurements across an ultra-wide concentration range through optimizing combined-segments strategy. *Sensors and Actuators B: Chemical* **423**, 136788, doi:<https://doi.org/10.1016/j.snb.2024.136788> (2025).
- 5 Babicheva, V. E. & Evlyukhin, A. B. Mie-resonant metaphotonics. *Adv. Opt. Photon.* **16**, 539-658, doi:10.1364/AOP.510826 (2024).
- 6 Kuznetsov, A. I., Miroshnichenko, A. E., Brongersma, M. L., Kivshar, Y. S. & Luk'yanchuk, B. Optically resonant dielectric nanostructures. *Science* **354**, aag2472, doi:10.1126/science.aag2472 (2016).
- 7 Wu, M. *et al.* Room-Temperature Lasing in Colloidal Nanoplatelets via Mie-Resonant Bound States in the Continuum. *Nano Letters* **20**, 6005-6011, doi:10.1021/acs.nanolett.0c01975 (2020).
- 8 Yao, K. *et al.* Tuning Multipolar Mie Scattering of Particles on a Dielectric-Covered Mirror. *ACS Nano* **18**, 16545-16555, doi:10.1021/acsnano.3c12893 (2024).
- 9 Zurita-Sánchez, J. R. Anapole arising from a Mie scatterer with dipole excitation. *Physical Review Research* **1**, 033064, doi:10.1103/PhysRevResearch.1.033064 (2019).
- 10 Baek, K., Kim, Y., Mohd-Noor, S. & Hyun, J. K. Mie Resonant Structural Colors. *ACS Applied Materials & Interfaces* **12**, 5300-5318, doi:10.1021/acsami.9b16683 (2020).
- 11 Yang, W. *et al.* All-dielectric metasurface for high-performance structural color. *Nature Communications* **11**, 1864, doi:10.1038/s41467-020-15773-0 (2020).
- 12 Goh, X. M. *et al.* Three-dimensional plasmonic stereoscopic prints in full colour. *Nature Communications* **5**, 5361, doi:10.1038/ncomms6361 (2014).
- 13 Dong, Z. *et al.* Ultraviolet Interband Plasmonics With Si Nanostructures. *Nano Letters* **19**, 8040-8048, doi:10.1021/acs.nanolett.9b03243 (2019).
- 14 Shamkhi, H. K. *et al.* Transverse Scattering and Generalized Kerker Effects in All-Dielectric Mie-Resonant Metaoptics. *Physical Review Letters* **122**, 193905, doi:10.1103/PhysRevLett.122.193905 (2019).
- 15 Fang, J. *et al.* Directional Modulation of Exciton Emission Using Single Dielectric Nanospheres. *Advanced Materials* **33**, 2007236, doi:<https://doi.org/10.1002/adma.202007236> (2021).
- 16 Zhang, F. *et al.* Non-Hermitian singularities in scattering spectra of Mie resonators. *Science Advances* **11**, eadr9183, doi:doi:10.1126/sciadv.adr9183 (2025).
- 17 Zhan, A. *et al.* Controlling three-dimensional optical fields via inverse Mie scattering. *Science Advances* **5**, eaax4769, doi:doi:10.1126/sciadv.aax4769 (2019).
- 18 Mie, G. Beiträge zur Optik trüber Medien, speziell kolloidaler Metallösungen. *Annalen der Physik* **330**, 377-445, doi:<https://doi.org/10.1002/andp.19083300302> (1908).
- 19 Hentschel, M. *et al.* Dielectric Mie voids: confining light in air. *Light: Science & Applications* **12**, 3, doi:10.1038/s41377-022-01015-z (2023).
- 20 Ossiander, M. *et al.* Extreme ultraviolet metalens by vacuum guiding. *Science* **380**, 59-63, doi:doi:10.1126/science.adg6881 (2023).

21 Vaskin, A., Kolkowski, R., Koenderink, A. F. & Staude, I. Light-emitting metasurfaces. *Nanophotonics* **8**, 1151-1198, doi:doi:10.1515/nanoph-2019-0110 (2019).

22 Ludescher, D. *et al.* Optical sieve for nanoplastic detection, sizing and counting. *Nature Photonics*, doi:10.1038/s41566-025-01733-x (2025).

23 Loudon, R. *The quantum theory of light*. 3rd Ed edn, (Oxford University Press, 2000).

24 Fu, Y., Huang, M. & Li, W. Spatial intensity distribution model of fluorescence emission considering the spatial attenuation effect of excitation light. *Opt. Express* **29**, 6468-6480, doi:10.1364/OE.416452 (2021).

25 Pelton, M. Modified spontaneous emission in nanophotonic structures. *Nature Photonics* **9**, 427-435, doi:10.1038/nphoton.2015.103 (2015).

26 Noda, S., Fujita, M. & Asano, T. Spontaneous-emission control by photonic crystals and nanocavities. *Nature Photonics* **1**, 449-458, doi:10.1038/nphoton.2007.141 (2007).

27 Russell, K. J., Liu, T.-L., Cui, S. & Hu, E. L. Large spontaneous emission enhancement in plasmonic nanocavities. *Nature Photonics* **6**, 459-462, doi:10.1038/nphoton.2012.112 (2012).

28 Purcell, E. M., Torrey, H. C. & Pound, R. V. Resonance Absorption by Nuclear Magnetic Moments in a Solid. *Physical Review* **69**, 37-38, doi:10.1103/PhysRev.69.37 (1946).

29 Vahala, K. J. Optical microcavities. *Nature* **424**, 839-846, doi:10.1038/nature01939 (2003).

30 Sauvan, C., Hugonin, J. P., Maksymov, I. S. & Lalanne, P. Theory of the Spontaneous Optical Emission of Nanosize Photonic and Plasmon Resonators. *Physical Review Letters* **110**, 237401, doi:10.1103/PhysRevLett.110.237401 (2013).

31 Sortino, L. *et al.* Enhanced light-matter interaction in an atomically thin semiconductor coupled with dielectric nano-antennas. *Nature Communications* **10**, 5119, doi:10.1038/s41467-019-12963-3 (2019).

32 Akselrod, G. M. *et al.* Probing the mechanisms of large Purcell enhancement in plasmonic nanoantennas. *Nature Photonics* **8**, 835-840, doi:10.1038/nphoton.2014.228 (2014).

33 Khatua, S. *et al.* Resonant Plasmonic Enhancement of Single-Molecule Fluorescence by Individual Gold Nanorods. *ACS Nano* **8**, 4440-4449, doi:10.1021/nn406434y (2014).

34 Schuller, J. A. *et al.* Plasmonics for extreme light concentration and manipulation. *Nature Materials* **9**, 193-204, doi:10.1038/nmat2630 (2010).

35 Kravets, V. G., Kabashin, A. V., Barnes, W. L. & Grigorenko, A. N. Plasmonic Surface Lattice Resonances: A Review of Properties and Applications. *Chemical Reviews* **118**, 5912-5951, doi:10.1021/acs.chemrev.8b00243 (2018).

36 Xiong, Y. *et al.* Photonic crystal enhanced fluorescence emission and blinking suppression for single quantum dot digital resolution biosensing. *Nature Communications* **13**, 4647, doi:10.1038/s41467-022-32387-w (2022).

37 Kuruma, K. *et al.* Coupling of a single tin-vacancy center to a photonic crystal cavity in diamond. *Applied Physics Letters* **118**, doi:10.1063/5.0051675 (2021).

38 Barreda, A., Mercadé, L., Zapata-Herrera, M., Aizpurua, J. & Martínez, A. Hybrid Photonic-Plasmonic Cavity Design for Very Large Purcell Factors at Telecommunication Wavelengths. *Physical Review Applied* **18**, 044066, doi:10.1103/PhysRevApplied.18.044066 (2022).

39 Adachi, M. *et al.* Fluorophore-Decorated Mie Resonant Silicon Nanosphere for Scattering/Fluorescence Dual-Mode Imaging. *Small* **19**, 2207318, doi:<https://doi.org/10.1002/smll.202207318> (2023).

40 Wang, Z., Wan, S., Shi, Y. & Li, Z. Vectorial Fluorescence Control with Light-Emitting Metasurfaces for Unidirectional Emission and Incoherent Holography. *Advanced Materials* **37**, 2502682, doi:<https://doi.org/10.1002/adma.202502682> (2025).

41 Kulkarni, S. P., Pathak, A. K., Krishnaswamy, S. & Aydin, K. High-Q Emission from Colloidal Quantum Dots Embedded in Polymer Quasi-BIC Metasurfaces. *Nano Letters* **25**, 1653-1659, doi:10.1021/acs.nanolett.4c05817 (2025).

42 Wu, S., Xia, H., Xu, J., Sun, X. & Liu, X. Manipulating Luminescence of Light Emitters by Photonic Crystals. *Advanced Materials* **30**, 1803362, doi:<https://doi.org/10.1002/adma.201803362> (2018).

43 Yuan, S. *et al.* Strong Photoluminescence Enhancement in All-Dielectric Fano Metasurface with High Quality Factor. *ACS Nano* **11**, 10704-10711, doi:10.1021/acsnano.7b04810 (2017).

44 Córdova-Castro, R. M. *et al.* Single-emitter super-resolved imaging of radiative decay rate enhancement in dielectric gap nanoantennas. *Light: Science & Applications* **13**, 7, doi:10.1038/s41377-023-01349-2 (2024).

45 Holsteen, A. L., Raza, S., Fan, P., Kik, P. G. & Brongersma, M. L. Purcell effect for active tuning of light scattering from semiconductor optical antennas. *Science* **358**, 1407-1410, doi:doi:10.1126/science.aa05371 (2017).

46 Tiguntseva, E. *et al.* Room-Temperature Lasing from Mie-Resonant Nonplasmonic Nanoparticles. *ACS Nano* **14**, 8149-8156, doi:10.1021/acsnano.0c01468 (2020).

47 Zhao, W. *et al.* Enhanced detection of fluorescence fluctuations for high-throughput super-resolution imaging. *Nature Photonics* **17**, 806-813, doi:10.1038/s41566-023-01234-9 (2023).

48 Curto, A. G. *et al.* Unidirectional Emission of a Quantum Dot Coupled to a Nanoantenna. *Science* **329**, 930-933, doi:doi:10.1126/science.1191922 (2010).

49 Ramakrishnan, S. B. *et al.* Cupric Oxide Mie Resonators. *The Journal of Physical Chemistry C* **126**, 16272-16279, doi:10.1021/acs.jpcc.2c04646 (2022).

50 Ren, J., Franke, S. & Hughes, S. Quasinormal Modes, Local Density of States, and Classical Purcell Factors for Coupled Loss-Gain Resonators. *Physical Review X* **11**, 041020, doi:10.1103/PhysRevX.11.041020 (2021).

51 Hamidi, M. *et al.* Quasi-Babinet principle in dielectric resonators and Mie voids. *Physical Review Research* **7**, 013136, doi:10.1103/PhysRevResearch.7.013136 (2025).

52 Conteduca, D. *et al.* Dielectric nanohole array metasurface for high-resolution near-field sensing and imaging. *Nature Communications* **12**, 3293, doi:10.1038/s41467-021-23357-9 (2021).

53 Athanasiou, S. & Martin, O. J. F. Alternative Plasmonic Materials for Fluorescence Enhancement. *The Journal of Physical Chemistry C* **128**, 18574-18581, doi:10.1021/acs.jpcc.4c05322 (2024).

54 Oh, J. W. *et al.* Dual-light emitting 3D encryption with printable fluorescent-phosphorescent metal-organic frameworks. *Light: Science & Applications* **12**, 226, doi:10.1038/s41377-023-01274-4 (2023).

55 Barulin, A. *et al.* Dual-wavelength metalens enables Epi-fluorescence detection from single molecules. *Nature Communications* **15**, 26, doi:10.1038/s41467-023-44407-4 (2024).

56 Adi, W. *et al.* Trapping light in air with membrane metasurfaces for vibrational strong coupling. *Nature Communications* **15**, 10049, doi:10.1038/s41467-024-54284-0 (2024).

57 Liu, H. *et al.* Tunable Resonator-Upconverted Emission (TRUE) Color Printing and Applications in Optical Security. *Advanced Materials* **31**, 1807900, doi:<https://doi.org/10.1002/adma.201807900> (2019).

58 García-Guirado, J., Svedendahl, M., Puigdollers, J. & Quidant, R. Enhanced Chiral Sensing with Dielectric Nanoresonators. *Nano Letters* **20**, 585-591, doi:10.1021/acs.nanolett.9b04334 (2020).

59 Kivshar, Y. The Rise of Mie-tronics. *Nano Letters* **22**, 3513-3515, doi:10.1021/acs.nanolett.2c00548 (2022).

60 Yavas, O., Svedendahl, M., Dobosz, P., Sanz, V. & Quidant, R. On-a-chip Biosensing Based on All-Dielectric Nanoresonators. *Nano Letters* **17**, 4421-4426, doi:10.1021/acs.nanolett.7b01518 (2017).

61 Badloe, T. *et al.* Liquid crystal-powered Mie resonators for electrically tunable photorealistic color gradients and dark blacks. *Light: Science & Applications* **11**, 118, doi:10.1038/s41377-022-00806-8 (2022).

62 Athanasiou, S. & Martin, O. J. F. Tuning Molecular Emission: Exploring Plasmonic Coupling Effects across High and Low Quantum Yields. *The Journal of Physical Chemistry C* **129**, 4282-4289, doi:10.1021/acs.jpcc.4c08617 (2025).

63 Ben Doudou, B., Chiba, I. & Daoues, H. S. Optical and thermo-optical properties of polyvinyl alcohol/carbon nanotubes composites investigated by prism coupling technique. *Optical Materials* **131**, 112672, doi:<https://doi.org/10.1016/j.optmat.2022.112672> (2022).

64 Liu, L., Wang, R., Sun, Y., Jin, Y. & Wu, A. Fluorescence enhancement of PbS colloidal quantum dots from silicon metasurfaces sustaining bound states in the continuum. *Nanophotonics* **12**, 3159-3164, doi:doi:10.1515/nanoph-2023-0195 (2023).

65 Chen, W. T. *et al.* High-Efficiency Broadband Meta-Hologram with Polarization-Controlled Dual Images. *Nano Letters* **14**, 225-230, doi:10.1021/nl403811d (2014).

66 Kumar, K. *et al.* Printing colour at the optical diffraction limit. *Nature Nanotechnology* **7**, 557-561, doi:10.1038/nnano.2012.128 (2012).

Data availability

All data involved in this work are included in this article and the corresponding supplementary materials.

Acknowledgment

The authors thank Dr. Stavros Athanasiou and Dr. Parmenion Mavrikakis for fruitful discussions. Funding from the Swiss National Science Foundation under grants 200021_212758 and CRSK-2_228838 is gratefully acknowledged. We also acknowledge support from the National Natural Science Foundation of China under grants 62405177 and the Outstanding Doctoral Graduates Development Scholarship of Shanghai Jiao Tong University.

Author contributions

Conceptualization: YF, OJFM;
Methodology: YF, IL, SB, MC, OJFM;
Investigation: YF, NZ, OJFM;
Visualization: YF, NZ;
Supervision: SB, SZ, TL, OJFM;
Writing—original draft: YF, IL, OJFM;
Writing—review & editing: YF, IL, SB, TL, SZ, MC, OJFM.

Competing interests

Authors declare that they have no competing interests.